Electrocatalysis

DOI: 10.1002/ange.201403363

Strongly Veined Carbon Nanoleaves as a Highly Efficient Metal-Free Electrocatalyst**

Tian-Nan Ye, Li-Bing Lv, Xin-Hao Li, Miao Xu, and Jie-Sheng Chen**

Abstract: *Effective integration of one-dimensional carbon nanofibers (CNF) and two-dimensional carbon sheets into three-dimensional (3D) conductive frameworks is essential for their practical applications as electrode materials. Herein, a novel "vein-leaf"-type 3D complex of carbon nanofibers with nitrogen-doped graphene (NG) was prepared through a simple thermal condensation of urea and bacterial cellulose. During the formation of the 3D complex CNF@NG, the graphene species was tethered to CNF via carbon–carbon bonds. Such an interconnected 3D network facilitates both the electron transfer and mass diffusion for electrochemical reactions.*

The lack of cheap, stable, and effective catalysts for the oxygen reduction reaction (ORR) at the cathode is still the main hurdle for the widespread application of proton-exchange-membrane (PEM) fuel cells.[1] With respect to the mainstream catalysts for PEM fuel cells, today's platinum-based catalysts suffer from high cost, limited stability, fast deactivation, and sluggish kinetics, which must be overcome for commercialization.[2] Great efforts have been devoted to synthesizing catalysts with an activity at least comparable to that of Pt but with higher durability and at much lower cost.[3] Carbon nanomaterials are cheap and stable, and are thus considered to be among the most promising alternative catalysts.[4] To date, the most developed carbon-based catalysts are the doped nanocarbon materials, including nanotubes, graphene, graphite materials, and nanodiamonds, whilst primitive carbon materials are less active or inert for ORR.[5] Heteroatom doping can strengthen the initial chemical adsorption of oxygen on the surface of the catalyst and also supply the possible active sites for oxygen reduction.[6] However, the incorporation of heteroatoms would directly tune the position of the conduction and/or valence band of the doped carbon material and thus lead to an opened bandgap, generating an intrinsic barrier that hinders charge transfer.[7]

The direct approach for balancing the competition between concentrations of active sites and conductivity is the integration of doped nanocarbon materials with highly conductive frameworks.[8] Recently, doped graphene as the active component for ORR in combination with porous carbon materials or nanotubes was shown to promote the electron transfer to the active sites, promising the advantages of nanocarbon blends for largely enhanced electrocatalytic activity.[5c,9] There is a consensus in the literature that tough contact nanocarbon complexes with abundant active sites and high conductivity are of critical for the final electrocatalytic activity.[10] In principle, the ideal contact for better electron transfer is the bonded interface connected by carbon–carbon bonds to form a conjugated three-dimensional (3D) network. Despite great efforts, constructing seamlessly connected nanocarbon composites via carbon–carbon bonds still remains a great challenge.

In this work, we developed a simple but effective method to construct highly integrated carbon nanofiber@nitrogen-doped graphene blends (CNF@NG). It is interesting that a "vein-leaf"-type 3D complex with carbon nanofibers as the skeleton and nitrogen-doped graphene as the leaf was obtained through simple calcination of a mixture of urea and bacterial cellulose (BC) (Figures 1 and S1), both of which are cheap, abundant, and sustainable biomass. The merging of hard and conductive carbon nanofibers with soft and active nitrogen-doped graphene via carbon–carbon bonds results in robust 3D networks that favor both the mass transfer from the electrolyte to the electrodes as well as the electron transfer to the active sites and then to the adsorbed oxygen molecules. The advantages of such a CNF@NG 3D network as electrochemical catalyst were finally reflected by the superior activity and stability in the oxygen reduction reaction in alkaline media, in which an activity comparable to that of Pt/C but a much better stability and methanol tolerance was observed.

Both urea and BC play multiple roles in the formation of such a unique "vein-leaf" structure. The fabrication process for CNF@NG complexes is demonstrated in Figure 1 and further details can be found in Figure S1. Urea was added as the nitrogen source and also the precursor of layered graphitic carbon nitride (g-C_3N_4) (Figure S2), which serves as a sacrificial template for the formation of graphene nanosheets in the interlayer voids (Figure 1b,c). The interconnected 3D scaffold (Figures 1a and S1a) of BC pellicles was chosen as the precursor for in situ carbonization into carbon nanofibers (CNF) (Figure S3a). The carbon intermediates generated from the carbonization of BC diffused into adjacent interlayer voids of g-C_3N_4 and were then thermally condensed into graphene nanosheets due to the confinement of the layered g-C_3N_4. Since the g-C_3N_4 template undergoes complete thermolysis at 680 °C (Figure S4), the final CNF@NG 3D network was then released at 900 °C (Figure 1c). When BC was

[*] T. N. Ye, L. B. Lv, Prof. X. H. Li, M. Xu, Prof. J. S. Chen
School of Chemistry and Chemical Engineering
Shanghai Jiao Tong University
Shanghai 200240 (P. R. China)
E-mail: xinhaoli@sjtu.edu.cn
chemcj@sjtu.edu.cn

[**] This work was financially supported by the National Basic Research Program of China (2013CB934102, 2011CB808703) and the National Natural Science Foundation of China.

Supporting information for this article is available on the WWW under http://dx.doi.org/10.1002/anie.201403363.

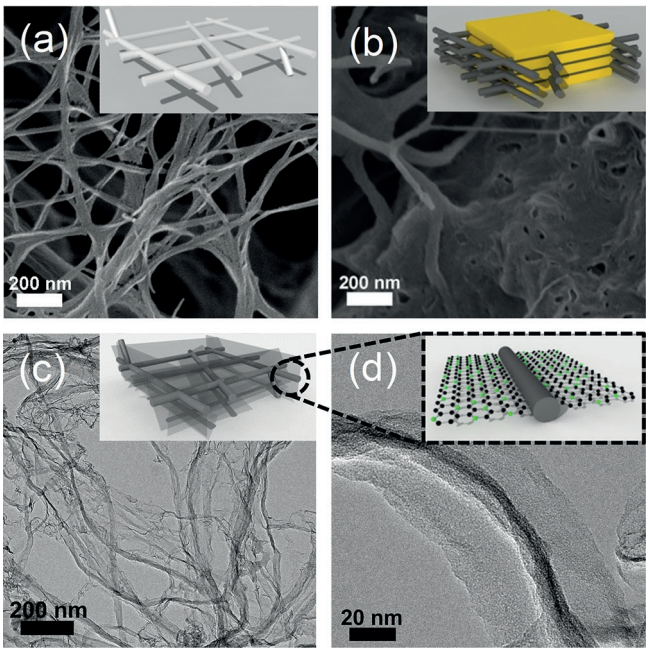

Figure 1. The synthesis of CNF@NG 3D complexes. a) The freeze-dried bacterial cellulose (BC) monolith (white rods) with an interpenetrating 3D network structure. b) The carbonized BC (CNF, black rods) wrapped by the g-C_3N_4 sacrifice template (yellow) after thermal condensation of the mixture of BC and urea at 600 °C resulting in the CNF@g-C_3N_4 hybrid. c) The CNF@NG was released after removal of g-C_3N_4 by heating at 900 °C. d) The amplified view of CNF@NG. Carbon atoms are black or gray and nitrogen atoms are green.

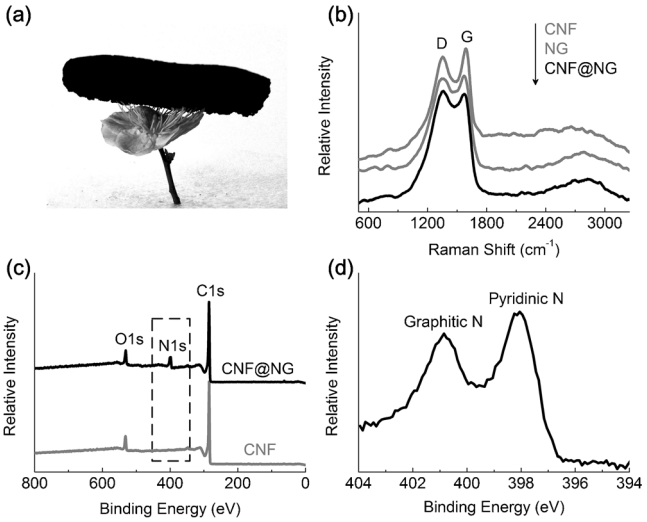

Figure 2. Compositional characterization of CNF@NG. a) Photograph of an CNF@NG aerogel with a low density (7.3 mg cm^{-3}) lying on a flower. b) Raman spectra of CNF, NG, and CNF@NG samples. c) XPS survey spectra of CNF and CNF@NG. d) High-resolution N 1s spectrum of CNF@NG with the peak deconvoluted into graphitic N and pyridinic N peaks.

replaced with glucose, a nitrogen-doped graphene (NG) monolith was obtained as a control sample.

The obtained CNF@NG aerogels are extremely light with a density as low as 7–8 mg cm^{-3} (Figure 2a), suggesting the well-preserved 3D structure of BC after thermal condensation, which can be further confirmed by the scanning electron microscope (SEM) images (Figure S3b). The enlarged transmission electron microscopy (TEM) images further demonstrated that the graphene pieces or nanoribbons were attached to both sides of the carbon nanofibers (Figure 1d) thereby forming a "vein-leaf" structure on the nanoscale. A number of graphene nanoribbons were completely or partially torn off from CNF due to the strong ultrasonication used for preparing the dispersion for TEM (Figure S5a) and atomic force microscopy (AFM) observation (Figure S6). On the basis of the AFM images, the thickness of these graphene nanosheets was estimated to be between 0.35 and 1.32 nm (Figure S6), indicating the formation of one to five layers. Brunauer–Emmett–Teller (BET) analysis showed that the specific surface area of CNF@NG (206 m^2 g^{-1}) is higher than that of bare CNF (132.9 m^2 g^{-1}) due to the presence of graphene nanosheets with a high surface area (782 m^2 g^{-1}) (Figure S7). The Raman spectrum (Figure 2b) of the CNF@NG sample further revealed the formation of graphitic carbon with a G-band at 1578 cm^{-1}. The D-bands centered at 1360 cm^{-1} and the trend of D/G ratios (CNF@NG $\approx$ NG > CNF) reflected the presence of defects or covalent modifications (e.g. C–N bonds) of the sp^2 carbon in CNF@NG and NG. X-ray photoelectron spectroscopy (XPS) analysis revealed the successful introduction of nitrogen atoms into the structure of CNF@NG. The content of N dopant was estimated to be 9.82 atom% according to the XPS analysis (Figure 2c). A certain amount of oxygen was also detected in CNF@NG, NG, and CNF obtained under similar conditions (Figure S8), which could be attributed to adsorbed oxygen-containing molecules as is well discussed in the literature.[11] The high-resolution N 1s XPS spectrum of CNF@NG demonstrated the presence of graphitic N and pyridinic N, both of which have been proven to result in highly active electrocatalytic sites for oxygen reduction in graphene networks (Figure 2d).[12] It is worth noting that the percentage of graphitic N in CNF@NG is much higher than that in post-treated graphite-oxide-based electrocatalysts, demonstrating a better distribution of heteroatoms in the sp^2 carbon network obtained by bottom-up methods, for example, the method described here.

We investigated the electrocatalytic performance of ORR as a model reaction over CNF@NG and a series of control samples including CNF, NG, a mechanical mixture of CNF and NG (CNF + NG), and the commercial 20 wt% Pt/C catalyst (Pt/C). As shown in Figure 3a, CNF@NG exhibited a very high limited current density of 5.0 mA cm^{-2} at 0.4 V vs. reversible hydrogen electrode (RHE), which is much higher than those of NG (2.5 mA cm^{-2}), CNF + NG (1.4 mA cm^{-2}), and CNF (1.2 mA cm^{-2}) (Figure 3b). Accordingly, the mass activity of the CNF@NG catalyst (5.39 A g^{-1} at 0.8 V vs. RHE) was 6.7 and 24.7 times higher than that of NG and CNF + NG, respectively, whilst the CNF catalyst was inactive at that potential (Figure S9). This trend was also reflected by the cyclic voltammetry (CV) results (Figure S10) where CNF@NG has the highest cathodic peak current and more positive ORR onset potential. The significantly more positive

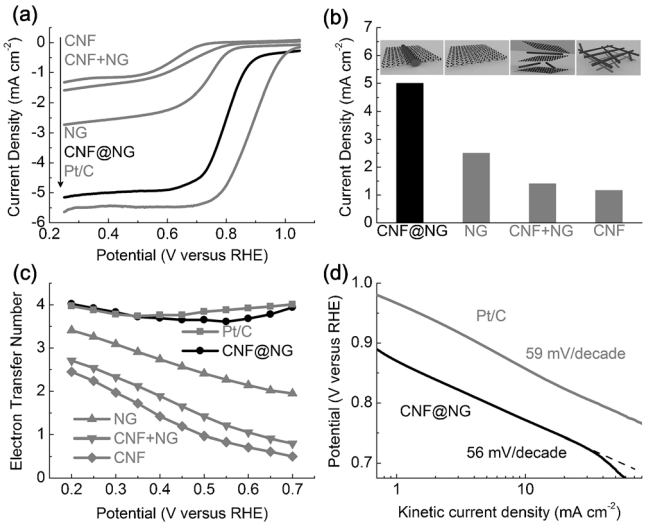

Figure 3. Electrochemical activity of the catalysts. a) Polarization curves of various electrocatalysts on glassy carbon electrodes at 1600 rpm in O_2-saturated 0.1 mol L^{-1} KOH solution with a sweep rate of 10 mV s^{-1}. The catalyst loading was 0.45 mg cm^{-2} for all samples. b) Limited current density of various electrocatalysts at 0.4 V vs. RHE; insets: the corresponding schemes. c) The electron transfer number (n) of various electrocatalysts as a function of the overpotential. d) The diffusion-current-corrected Tafel plots of CNF@NG and Pt/C catalysts.

onset potential on CNF@NG (0.93 V vs. RHE), which is only ca. 0.1 V more negative than that on the commercial Pt/C catalyst, suggests the excellent electrocatalytic activity of CNF@NG. A high working potential should be maintained at the cathode of fuel cells and air batteries to ensure a high energy conversion efficiency, which can be directly reflected by the ORR half-wave potential $E_{1/2}$.[13] It is worth noting that CNF@NG manifested an $E_{1/2}$ of (0.80 ± 0.02) V vs. RHE, making it one of the most active metal-free ORR catalysts (Table S1).[5a–d,6c–e,9,14]

Care should be taken when discussing the catalytic performance of metal-free electrocatalysts. It has been demonstrated that a trace amount of metal will result in an obvious positive shift in the $E_{1/2}$ and also increase current output. In order to avoid the involvement of metal species, we carefully control the synthetic process by using high-purity reagents and water and a high-quality corundum crucible as the reactor during the synthetic process. Besides carbon, nitrogen and, oxygen, no other elements were detected via XPS and ICP analysis, revealing the metal-free nature of CNF@NG. Moreover, both the CNF and NG obtained under similar conditions, exhibit a more negative $E_{1/2}$ (Figure 3a), which unambiguously excludes the involvement of electrocatalytically active metal species in the samples obtained in our synthetic system.

Metal-free electrocatalysts usually suffer from poor electron transfer to the adsorbed oxygen molecules and thus low selectivity for the four-electron reduction of oxygen. Two-electron reduction of oxygen may also occur but is less desirable due to the low efficiency and the corrosive nature of the resulting hydrogen peroxide. The electron transfer numbers (n) per oxygen molecule of the different samples were calculated on the basis of Koutecky–Levich (K-L) plots (Figures 3c and S11a-b) transferred from the polarization curves at various rotation speeds (Figure S12). The n value for CNF@NG is between 3.6 and 4.0 over the potential range from 0.2 V to 0.7 V vs RHE, thereby indicating a more efficient $4e^-$-dominated ORR process, with a performance approaching that of Pt/C catalysts. In contrast, NG shows an n value of 2.2–3.4, evidencing a combined pathway of $2e^-$ and $4e^-$ reductions. Additionally, the $n \approx 1.0$–2.5 suggests that CNF + NG and CNF favor the $2e^-$ oxygen reduction process. The ORR Tafel slope measured with the CNF@NG catalyst is ca. 56 mV per decade (Figure 3d), which is close to the 59 mV per decade for the Pt/C catalyst measured in our current system, further demonstrating the excellent catalytic activity of CNF@NG. All these results indicated that the rationally constructed interconnected 3D complex is efficient and has the potential to make metal-free carbon even more "noble".

Due to the high thermal and chemical stability of CNF@NG obtained at high temperature, its durability for ORR is very high. As shown in Figure 4a, CNF@NG exhibited a very slow attenuation after 36000 s in

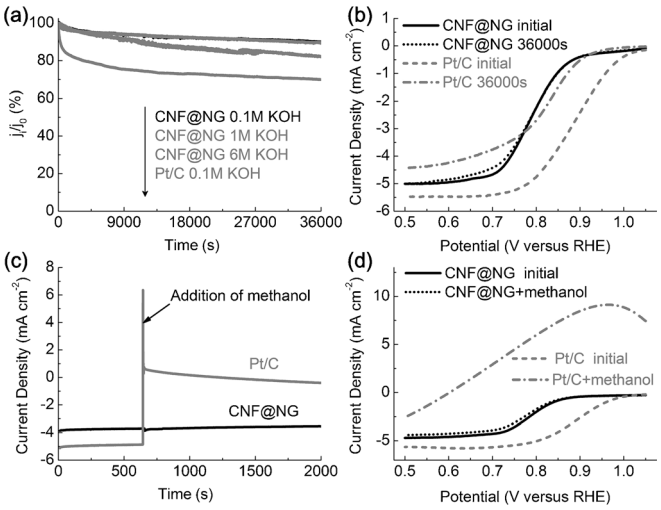

Figure 4. Electrochemical stability of the catalysts. a) Chronoamperometric response (i–t) at 0.4 V vs. RHE of CNF@NG catalyst in O_2-saturated 0.1 mol L^{-1}, 1 mol L^{-1}, and 6 mol L^{-1} KOH electrolyte and Pt/C in O_2-saturated 0.1 mol L^{-1} KOH electrolyte as reference. b) Polarization curves of CNF@NG and Pt/C before and after 36000 s in O_2-saturated electrolyte. c) Chronoamperometric responses (i–t) of CNF@NG and Pt/C at 0.4 V vs. RHE in O_2-saturated 0.1 mol L^{-1} KOH electrolyte. The arrow indicates the addition of methanol. d) Polarization curves of CNF@NG and Pt/C in O_2-saturated electrolyte before and after addition of methanol (final concentration: 3 mol L^{-1}).

0.1 mol L^{-1} KOH solution at which time 90.1 % of the relative current persisted, whereas Pt/C lost nearly 30 % of its initial activity. No obvious negative shift in the half-wave potential $E_{1/2}$ was observed for CNF@NG (Figure 4b). Moreover, the CNF@NG-based electrode can also survive in a highly corrosive electrolyte such as 1 mol L^{-1} and 6 mol L^{-1} KOH (Figure 4a), further confirming the reliable stability of CNF@NG for ORR. For direct use in methanol fuel cells,

ORR catalysts should also exhibit a satisfactory tolerance to the methanol that may pass across the membrane from the anode. As shown in Figure 4c, the original cathodic ORR current of CNF@NG was not obviously depressed by the crossover effect, whilst Pt/C exhibited a distinct methanol oxidation reaction after the introduction of methanol (Figure 4d). Indeed, CNF@NG is an ideal cathode catalyst for a direct methanol alkaline fuel cell.

To unveil the origin of the superior performance of CNF@NG in ORR, we further analyzed the structural features to determine the effect of the unique "vein-leaf" structure on the electron transfer and the mass transfer for ORR. The high-resolution transmission electron microscopy (HRTEM) image reveals that the two types of subunits, CNF and NG, were highly integrated via carbon–carbon bonds. Figure 5a shows the bonded structure of CNF@NG with the plane of NG naturally extended from the crystal lattice of CNF. The NG nanosheets grew along the carbon lattice of CNF, presumably due to the confinement effect inside the layers of the carbon nitride template. Further AFM observation (Figure S6c,d) unambiguously demonstrated the seamless connection between CNF and NG.

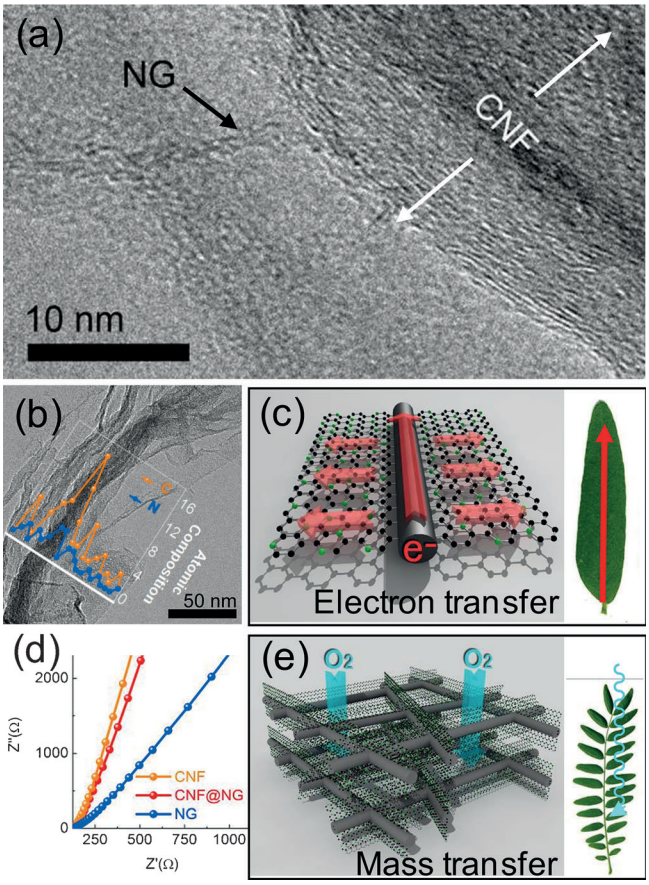

Figure 5. Structural and morphological characterization of the catalyst. a) HRTEM image of CNF@NG, CNF and NG are labeled. b) Compositional line profile across the CNF@NG. c) Scheme of CNF@NG "vein-leaf" complex structure for enhancing the electron transfer. (Carbon atoms are black or gray and nitrogen atoms are green). d) EIS spectra of CNF@NG, NG, and CNF in O_2-saturated KOH solution (0.1 mol L^{-1}). At a low frequency, the steeper slope indicated favorable transport. e) Scheme of the complex interpenetrated 3D network structure of CNF@NG, which facilitates the mass transfer (here exemplified with molecular oxygen).

Considering the unique interconnected 3D structure of CNF@NG, it is important to demonstrate the distribution of N dopants and thus the active sites in the "nanoleaves". Energy-dispersive X-ray spectroscopy (EDS) line scans revealed a homogeneous distribution of N atoms all over the "leaf" without obvious enrichment in certain areas (Figures 5b and S13). The CNF was found to be carbon-rich. As a result, the N content of CNF@NG (9.82 atom%) was only slightly lower than that of bare NG (10.7 atom%) as revealed by the XPS results (Figure S8), whilst the distribution of N atoms in the graphene plane is similar (Figure S14). This implies that the effect of nitrogen content and structure on the catalytic performance of CNF@NG was negligible as compared to that of bare NG. Moreover, the low N content (Figure 2c) and the sp^2 carbon networks of the CNF@NG sample (Figure 2b) rather suggest that the connections between CNF and NG are mainly in the form of C–C bonds. The interface resistance of the 3D monolith for electron transfer could be principally reduced as such. Indeed, the conductivity of the monolith of CNF@NG was a little bit higher than that of the bare CNF monolith, demonstrating the advantage of such a "leaf-vein" structure for electron transfer by following the principle of water transfer inside real leaves (Figure 5c).

The direct connection of the rigid CNF and the flexible NG nanosheets also makes CNF@NG monoliths robust enough to retain the porous 3D structure (Figures 1c and 5e) in liquid, favoring a better mass transfer for ORR. Due to the liquid capillary force between graphene and liquid and/or van der Waals forces between adjacent graphene layers, flexible graphenes tend to shrink in the liquid phase after multiple cycles. Consequently, the shrinkage of the graphene monolith results in lower porosity and closely packed aggregates, blocking the mass transfer to the inner part of the catalysts.[15] To glean this effect, we performed electrochemical impedance spectroscopy (EIS) for various catalysts (Figure 5d). As expected, the CNF@NG 3D network exhibited a much lower diffusion resistance than NG, which was comparable to bare CNF. In the same way that the structure of plants ensures that all leaves have access to light and gas, the voids among these nanoleaves and also the stick-backbone-integrated CNF assures the efficient mass transfer to the active sites and markedly facilitates ORR diffusion kinetics (Figure 5e).

In summary, we have demonstrated a simple method to prepare highly integrated carbon nanofiber@nitrogen-doped graphene "vein-leaf" 3D complexes connected by carbon–carbon bonds. The resulting CNF@NG catalyst exhibits high activity, excellent tolerance to methanol, and superior stability in alkaline solutions. The superb electrocatalytic activity and durability of the CNF@NG catalyst in ORR are attributed to the robust porous 3D structure, which favors both electron and mass transfer for ORR. Given that the precursors are all biomass (urea and cellulose), we believe that the present synthetic strategy can be further extended to the development of cheap functional hybrid materials for

large-scale applications, such as the fabrication of sensors, batteries, supercapacitors, and catalysts.

Received: March 15, 2014
Published online: May 22, 2014

Keywords: biomass · carbon nanofibers · electrocatalysts · graphene · leaf nanostructures

[1] M. K. Debe, *Nature* **2012**, *486*, 43 – 51.
[2] a) H. A. Gasteiger, S. S. Kocha, B. Sompalli, F. T. Wagner, *Appl. Catal. B* **2005**, *56*, 9 – 35; b) B. C. Steele, A. Heinzel, *Nature* **2001**, *414*, 345 – 352; c) M. Winter, R. J. Brodd, *Chem. Rev.* **2005**, *105*, 1021 – 1021.
[3] a) Y. Liang, Y. Li, H. Wang, J. Zhou, J. Wang, T. Regier, H. Dai, *Nat. Mater.* **2011**, *10*, 780 – 786; b) G. Wu, K. L. More, C. M. Johnston, P. Zelenay, *Science* **2011**, *332*, 443 – 447; c) D. S. Su, G. Sun, *Angew. Chem.* **2011**, *123*, 11774 – 11777; *Angew. Chem. Int. Ed.* **2011**, *50*, 11570 – 11572.
[4] a) K. Gong, F. Du, Z. Xia, M. Durstock, L. Dai, *Science* **2009**, *323*, 760 – 764; b) Y. Zhai, Y. Dou, D. Zhao, P. F. Fulvio, R. T. Mayes, S. Dai, *Adv. Mater.* **2011**, *23*, 4828 – 4850; c) D. S. Su, R. Schlögl, *ChemSusChem* **2010**, *3*, 136 – 168.
[5] a) L. Qu, Y. Liu, J. B. Baek, L. Dai, *ACS Nano* **2010**, *4*, 1321 – 1326; b) R. Silva, D. Voiry, M. Chhowalla, T. Asefa, *J. Am. Chem. Soc.* **2013**, *135*, 7823 – 7826; c) P. Chen, T. Y. Xiao, Y. H. Qian, S. S. Li, S. H. Yu, *Adv. Mater.* **2013**, *25*, 3192 – 3196; d) R. Liu, D. Wu, X. Feng, K. Müllen, *Angew. Chem.* **2010**, *122*, 2619 – 2623; *Angew. Chem. Int. Ed.* **2010**, *49*, 2565 – 2569; e) X. H. Li, S. Kurasch, U. Kaiser, M. Antonietti, *Angew. Chem.* **2012**, *124*, 9827 – 9830; *Angew. Chem. Int. Ed.* **2012**, *51*, 9689 – 9692; f) I. Y. Jeon, S. Zhang, L. Zhang, H. J. Choi, J. M. Seo, Z. Xia, L. Dai, J. B. Baek, *Adv. Mater.* **2013**, *25*, 6138 – 6145.
[6] a) S. Maldonado, K. J. Stevenson, *J. Phys. Chem. B* **2005**, *109*, 4707 – 4716; b) S. Chen, J. Bi, Y. Zhao, L. Yang, C. Zhang, Y. Ma, Q. Wu, X. Wang, Z. Hu, *Adv. Mater.* **2012**, *24*, 5593 – 5597; c) J. Liang, Y. Jiao, M. Jaroniec, S. Z. Qiao, *Angew. Chem.* **2012**, *124*, 11664 – 11668; *Angew. Chem. Int. Ed.* **2012**, *51*, 11496 – 11500; d) D. S. Yang, D. Bhattacharjya, S. Inamdar, J. Park, J. S. Yu, *J. Am. Chem. Soc.* **2012**, *134*, 16127 – 16130; e) S. Wang, L. Zhang, Z. Xia, A. Roy, D. W. Chang, J. B. Baek, L. Dai, *Angew. Chem.* **2012**, *124*, 4285 – 4288; *Angew. Chem. Int. Ed.* **2012**, *51*, 4209 – 4212.
[7] a) X. Wang, X. Li, L. Zhang, Y. Yoon, P. K. Weber, H. Wang, J. Guo, H. Dai, *Science* **2009**, *324*, 768 – 771; b) X. H. Li, M. Antonietti, *Angew. Chem.* **2013**, *125*, 4670 – 4674; *Angew. Chem. Int. Ed.* **2013**, *52*, 4572 – 4576; c) Y. Zhao, C. Hu, Y. Hu, H. Cheng, G. Shi, L. Qu, *Angew. Chem.* **2012**, *124*, 11533 – 11537; *Angew. Chem. Int. Ed.* **2012**, *51*, 11371 – 11375.
[8] a) Z. Chen, W. Ren, L. Gao, B. Liu, S. Pei, H. M. Cheng, *Nat. Mater.* **2011**, *10*, 424 – 428; b) K. S. Kim, Y. Zhao, H. Jang, S. Y. Lee, J. M. Kim, K. S. Kim, J. H. Ahn, P. Kim, J. Y. Choi, B. H. Hong, *Nature* **2009**, *457*, 706 – 710.
[9] J. Liang, X. Du, C. Gibson, X. W. Du, S. Z. Qiao, *Adv. Mater.* **2013**, *25*, 6226 – 6231.
[10] Y. Li, W. Zhou, H. Wang, L. Xie, Y. Liang, F. Wei, J. C. Idrobo, S. J. Pennycook, H. Dai, *Nat. Nanotechnol.* **2012**, *7*, 394 – 400.
[11] a) Y. Zhu, S. Murali, M. D. Stoller, K. Ganesh, W. Cai, P. J. Ferreira, A. Pirkle, R. M. Wallace, K. A. Cychosz, M. Thommes, *Science* **2011**, *332*, 1537 – 1541; b) Z. Niu, J. Chen, H. H. Hng, J. Ma, X. Chen, *Adv. Mater.* **2012**, *24*, 4144 – 4150.
[12] a) D. Geng, Y. Chen, Y. Chen, Y. Li, R. Li, X. Sun, S. Ye, S. Knights, *Energy Environ. Sci.* **2011**, *4*, 760 – 764; b) H. Wang, T. Maiyalagan, X. Wang, *ACS Catal.* **2012**, *2*, 781 – 794.
[13] a) R. Cao, R. Thapa, H. Kim, X. Xu, M. G. Kim, Q. Li, N. Park, M. Liu, J. Cho, *Nat. Commun.* **2013**, *4*, 2076; b) H. W. Liang, W. Wei, Z.-S. Wu, X. Feng, K. Müllen, *J. Am. Chem. Soc.* **2013**, *135*, 16002 – 16005.
[14] a) K. Parvez, S. Yang, Y. Hernandez, A. Winter, A. Turchanin, X. Feng, K. Müllen, *ACS Nano* **2012**, *6*, 9541 – 9550; b) Z. Yang, Z. Yao, G. Li, G. Fang, H. Nie, Z. Liu, X. Zhou, X. a. Chen, S. Huang, *ACS Nano* **2011**, *6*, 205 – 211.
[15] X. H. Li, X. Wang, M. Antonietti, *Chem. Sci.* **2012**, *3*, 2170 – 2174.

